# Supporting Information

# Experimental proof of concept of nanoparticle assisted STED

Yannick Sonnefraud,*,†,‡ Hugo G. Sinclair,¶ Yonatan Sivan,§ Matthew R. Foreman,‖ Christopher W. Dunsby,¶ Mark A. A. Neil,¶ Paul M. French,¶ and Stefan A. Maier‡

*Institut Néel, CNRS UPR 2940, 25 rue des Martyrs BP 166, 38042 Grenoble Cedex 9, Imperial College London, Blackett Laboratory, Experimental Solid State Group, SW7 2AZ London UK, Imperial College London, Blackett Laboratory, Photonics Group, SW7 2AZ London UK, Unit of electro-optics Engineering, Faculty of Engineering Science, Ben-Gurion University, Beer-Sheva, PO box 84105, and Max Planck Institute for the Science of Light, Laboratory of Nanophotonics & Biosensing, 91058 Erlangen, Germany*

E-mail: yannick.sonnefraud@neel.cnrs.fr

## STED microscope - experimental configuration

The STED microscope employed in this study has been described previously[1,2] and is based on a single 80 MHz Ti:Sapphire source tuned to 780 nm (Spectra-Physics Mai Tai HP).

*To whom correspondence should be addressed
†Institut Néel, CNRS
‡Imperial College London, Experimental Solid State Group
¶Imperial College London, Photonics Group
§Ben-Gurion University, Unit of electro-optics Engineering
‖Max Planck Institute, Erlangen

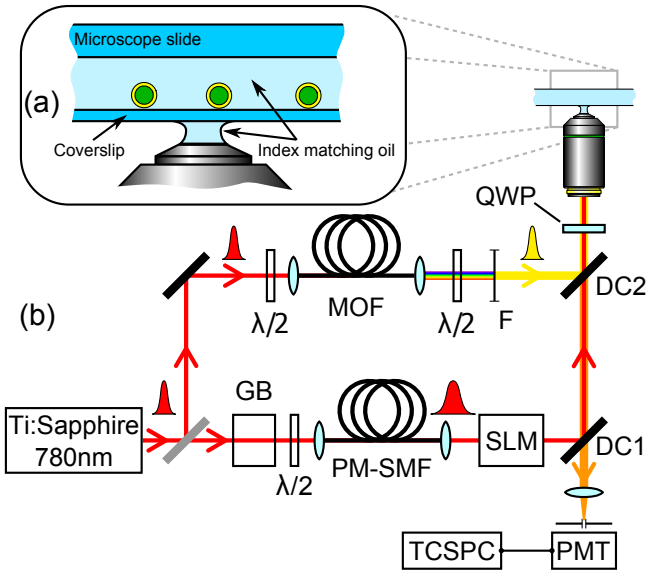


Figure S1: Experimental configuration. (a) Sample: the NPs are drop cast on a glass coverslip, immersed in index matching oil sandwiched between the coverslip and a microscope slide. (b) Description of the FLIM-STED nanoscopy setup. MOF: microstructured optical fibre, QWP: quarter wave plate, GB: 1 meter long SF57 glass block to stretch the pulse, PM-SMF: polarization maintaining single mode fiber, SLM: spatial light modulator, DC1 and DC2: dichroic mirrors, PMT: photomultiplier tube, TCSPC: time correlated single photon counting unit.

Figure S1b shows a schematic of the system. The beam exiting the laser source is split via a Glan-Taylor polarizer and half-wave plate to adjust the ratio of intensity going into the two beampaths. To provide excitation light, a portion of the beam is coupled into a microstructured optical fibre (MOF) in which a supercontinuum is formed spanning from ∼500 nm to above 1 micron. Band-pass filters (F) are then used to select an appropriate waveband from the supercontinuum. For the ATTO 647N fluorophore used in these experiments a 54 nm waveband centered at 609 nm was used for excitation. For depletion, the remaining pulses from the Ti:Sapphire are stretched from ∼100 fs to ∼300 ps using a combination of 1 meter of SF57 glass (GB) and 100 m of polarization maintaining single mode fibre (PM-SMF). The depletion beam is then modulated with a liquid crystal spatial light modulator (SLM, X10468-02, Hamamatsu) in order to impart the helical phase profile required to generate the doughnut for STED. The SLM is also used to correct for aberrations present in the depletion beam due to optical misalignments/imperfections. The excitation and deple-

tion beams are combined using dichroic mirrors (DC1 and DC2), circularly polarized via an achromatic quarter wave plate (QWP, Bernhard Halle) and focused into the sample with an 100×, $1.4NA$ Leica objective lens. The dichroic mirrors also serve to separate scattered excitation and depletion light from fluorescence excited in the sample. Residual scattered photons are filtered from the fluorescence signal via further bandpass filters. Fluorescence is coupled into a 50 $\mu$m-core fiber which acts as a confocal pinhole and is detected via a hybrid PMT(HPM-100-50, Becker & Hickl) connected to time correlated single photon counting electronics (SPC-830, Becker & Hickl). Sample scanning is performed via a 3-axis piezo stage (Mad City Labs, Madison).

## Resolution improvement, STED vs. NP-STED

Let's assume one wants to reach a specific resolution improvement $\chi$ using STED. Without the use of the bare cores only, $\chi$ is achieved with a STED power of $P_{STED} = P_1$. Similarly, using core-shell particles, let the power required be $P_{STED} = P_{cs}$. Then:

$$\chi = 100 \cdot \left(1 - \frac{1}{\sqrt{1 + \frac{P_1}{P_{sat}}}}\right) = 100 \cdot \left(1 - \frac{1}{\sqrt{1 + \Gamma_p \frac{P_{cs}}{P_{sat}}}}\right). \tag{1}$$

Which can be rewritten as:

$$\frac{1}{\sqrt{1 + \frac{P_1}{P_{sat}}}} = \frac{1}{\sqrt{1 + \Gamma_p \frac{P_{cs}}{P_{sat}}}}, \tag{2}$$

$$P_1 = \Gamma_p P_{cs}. \tag{3}$$

Thus the power required with the bare cores is $\Gamma_p$ times larger than the power required with the core-shells.

## Depletion curve

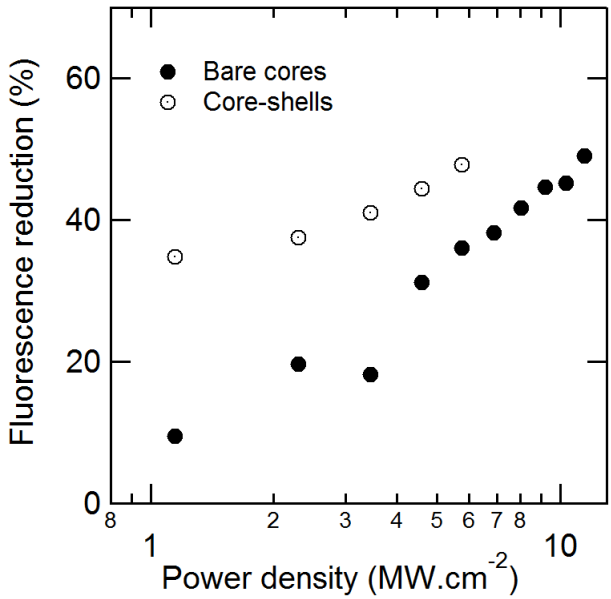


Figure S2: Depletion curve. The reduction in fluorescence intensity is measured as a function of depletion power density, for a population of nanoparticles.

Figure S2 presents the depletion vs. power density obtained for a population of nanoparticles, when the depletion beam used is a simple Gaussian beam. The experimental conditions are similar to that of the standard measurement, apart from the shape of the depletion beam. At each power three successive images are taken: a confocal image with depletion beam off, a STED image with both excitation and depletion beam on, and lastly an image with only the depletion beam on. In the case of the bare cores, the last image (depletion beam only) shows almost no intensity, whereas in the core-shell case it represents the parasitic luminescence of the gold. Then, the image with only the depletion beam active is subtracted from the standard STED image. The total counts across the confocal and the corrected image are compared in order to obtain the points of Fig. S2. In the case of the bare cores, the reduction in fluorescence intensity over the range studied is linear in logarithmic scale, whereas in the core-shell case it is not. Moreover, no data point above 6 MW.cm$^{-2}$ is shown because past this threshold the particles show signs of damage. The presence of the gold on

the nanoparticles does improve the depletion efficiency.

## Luminescence of gold

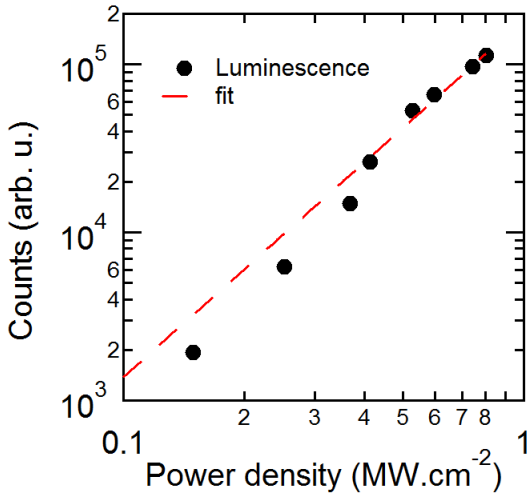


Figure S3: Luminescence of the core-shells as a function of power density (solid disks). To obtain the curve, only a Gaussian depletion beam was scanned over a collection of core-shells (fluorescence excitation off). The red dashed line is a fit to that curve to a power law with fitting coefficient of $\alpha = 2.12 \pm 0.13$.

Figure S3 shows the integrated luminescence collected from core-shell particles when only the depletion beam is used to excite them. The data has been fit to a function of the form $f(x) = Ax^{\alpha}$. The fit returns the value $\alpha = 2.12 \pm 0.13$, confirming that the process at the origin of the luminescence is probably a two photon absorption.

## Additional data on the resolution

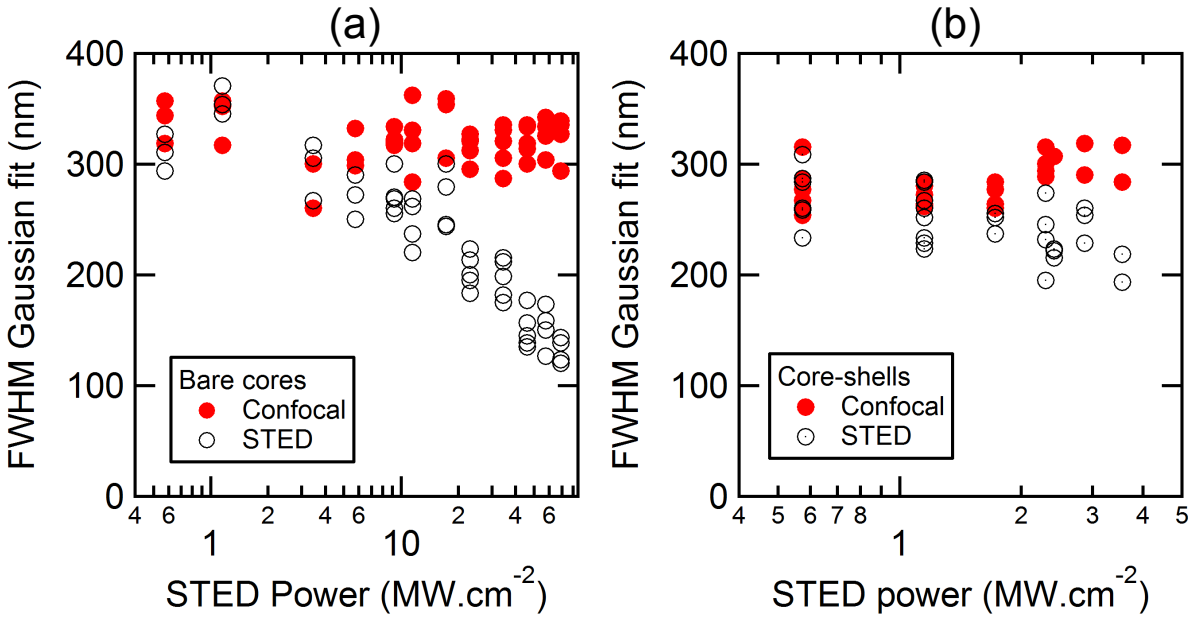


Figure S4: Measurement of the FWHM of the fluorescence spots used to calculate the resolution improvements in figure 3 of the article. (a) Resolution, taken as the FWHM of a Gaussian fit to the image for the bare cores, for confocal (red disks) and STED modes (black circles). (b) Same information for the core-shells: confocal (red disks) and STED (black circles). In every case, the signal has been time gated as indicated in the main text before calculating the resolution.

In this section we present more data on the calculation of the resolution improvement. Figure S4 shows the FWHM of the points measured to calculate the resolution improvement. The typical confocal resolution we obtain after time gating the signal is close to 300 nm. Figure S5.a is similar to Fig. 3 in the main text. In Fig. S5 the additional labels 1 through 6 refer to the plots shown below in the central and bottom panels, which give the data for six points of the graph. Figure S5.b presents the data in Fig. S5.a in the form of the mean resolution improvement (point position) and standard deviation (error bars) for each power density used. The middle and bottom panels show the confocal images (top left), time-gated STED image (top right), profiles (left curve) and corresponding Gaussian fits (right curves) to the profiles used to determine the resolution improvement. The white and red arrows indicate the positions where the profiles have been taken in the confocal and STED images

respectively. In the plots, the black (resp. red) curves correspond to data for the confocal images (resp. time gated STED images). Particles 2, 3 and 4 were captured in the same field of view and are shown together. In the case of 1, 5 and 6 the particles were alone in the field of view, so only a 1x1$\mu$m$^2$ range is shown. Every data set is for a different particle. Note that the particle presented in Fig. 2 in the main text is NP 2 in this figure, rotated 90° clockwise.

Figure S6 presents the profiles extracted from the same confocal and STED data, when the cut is done horizontally. In that direction, at high depletion power, there is often a halo that the time gating has not managed to completely get rid of. The intensity of the halo changes from particle to particle. In some cases (NP 4 and 5 for instance), when taking into account the halo the resolution becomes worse than in the confocal mode. In the other cases the improvement is not as good as when the cut is taken in the vertical direction, with some particles showing a more symmetric pattern (NP 3 for instance). S1 and S2 summarize the results.

Table S1: Resolution comparison confocal / STED with vertical profiles

| Particle number | Confocal width (nm) | STED width (nm) | Resolution improvement (%) |
|---|---|---|---|
| 1 | 158 | 140 | 11.4 |
| 2 | 189 | 164 | 13.2 |
| 3 | 173 | 139 | 19.7 |
| 4 | 180 | 117 | 35 |
| 5 | 174 | 137 | 21.3 |
| 6 | 190 | 116 | 38.9 |

Table S2: Resolution comparison confocal / STED with horizontal profiles

| Particle number | Confocal width (nm) | STED width (nm) | Resolution improvement (%) |
|---|---|---|---|
| 1 | 155 | 144 | 9.9 |
| 2 | 159 | 166 | 4.3 |
| 3 | 177 | 152 | 14 |
| 4 | 155 | 177 | -14 |
| 5 | 190 | 235 | -20 |
| 6 | 160 | 140 | 12.5 |

# Additional data on the theoretical modeling

We compared the measured resolution with that deduced theoretically, as described in,[3] for the geometrical parameters extracted from the TEM images. As shown in,[4] one first needs to determine the intensity enhancement distribution in space for every point in the scan, i.e., for every relative position of the NP and the doughnut center. The results of exact Mie calculations, shown in Fig. S7, indicate that the intensity enhancement within the core varies between 1 to 10 for different scan positions. As explained in,[3] where the field enhancement around metal core-shell NPs and its dependence on the illumination pattern were studied in detail, since the doughnut beam used in STED imaging has a true zero at its center, it *does not* have an electric dipole moment. Accordingly, the field enhancement level shifts from the enhancement appropriate to the next highest multipole moment in the beam (an electric quadrupole in the current case) for the case where the beam is centered on the NP to the enhancement appropriate to the electric dipole moment as the doughnut beam is scanned away from the metal NP. As a result, the efficient excitation of the quadrupolar mode makes the enhancement non-uniform. Moreover, the interference of the quadrupolar mode with the dipolar mode also generates some asymmetry, enabled by the specific handedness of the doughnut beam used. These aspects will be studied in more detail separately, but will be weaker once smaller particles will be used. Despite these issues, we show in Fig. S7 that the Point-Spread-Function (PSF), obtained by scanning a single core-shell NP (with a core full of emitters), shows no signs of distortion due to the non-uniformity of the enhancement. This

justifies the adoption of the standard STED interpretation of the shrunk PSF. Moreover, following,[5] we have averaged the intensity enhancement over the inner volume of the core, excluding a thin (10 nm) shell of the core which is assumed not to contribute to the overall signal due to quenching, see Fig. S7. The average intensity enhancement within the core of the nano-shell, as a function of the scan coordinate, is found to be roughly 4. Judging from the emission data and dark-field images (see Fig. 1), we estimate the decay rate enhancement to be negligible. Thus, the intensity reduction predicted theoretically, $\Gamma_p \approx 4$, is in good agreement with the measured value. Substitution of this value in the fit to the experimental STED data with the bare cores shows an excellent match to the fit to the experimental NP-STED data (not shown in order to avoid overflowing the experimental figures).

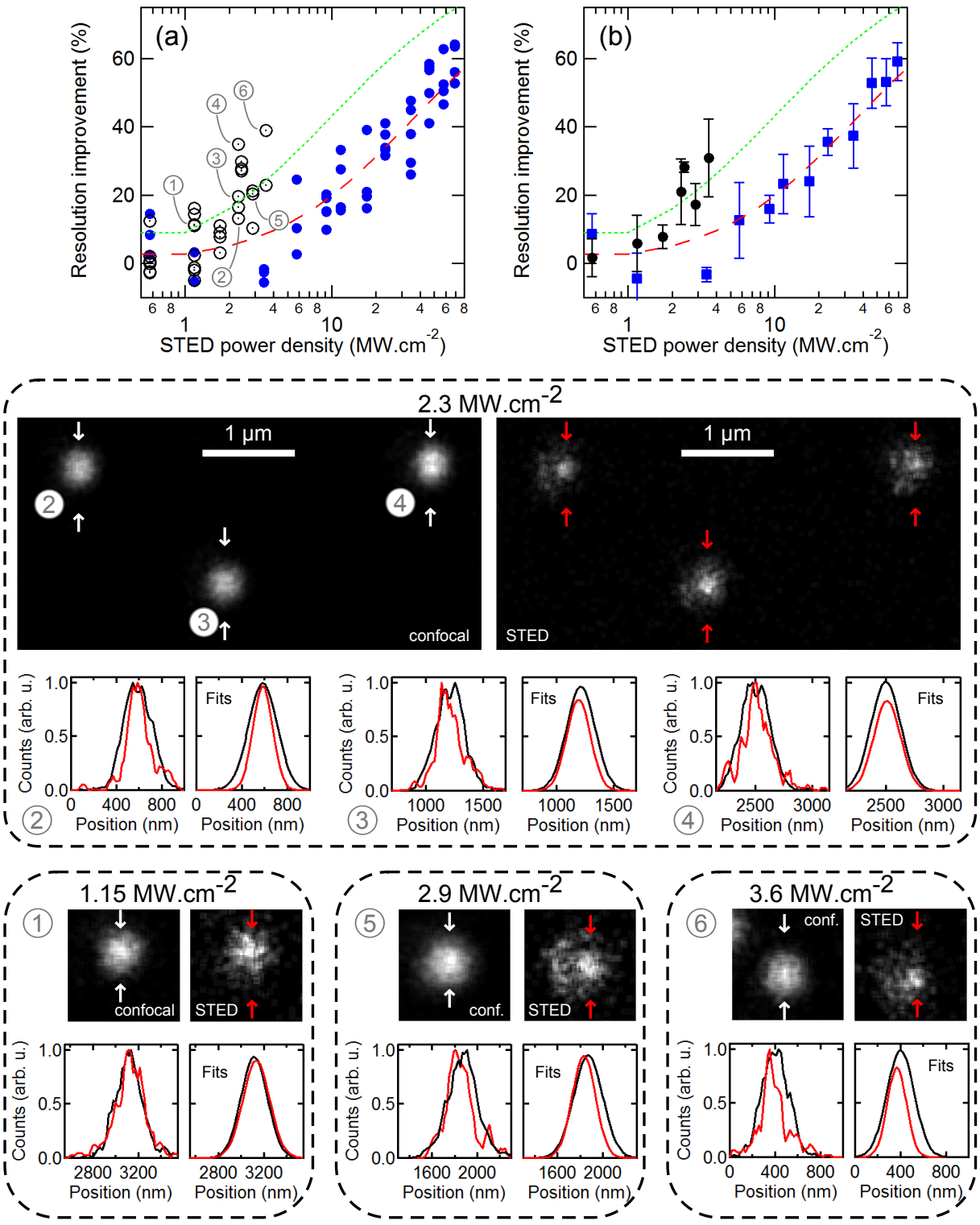


Figure S5: Additional experimental data; vertical profiles. (a) Same figure as figure 3 in the main text. (b) presents the same data, plotted as the mean improvement at the corresponding power density, and the error bars represent the standard deviation. Below is shown the data used to produce the points labeled 1 through 6 in (a). The scale bars for the middle panel is 1$\mu$m and the images corresponding to 1, 5 and 6 are 1x1$\mu$m$^2$. See text for more details.

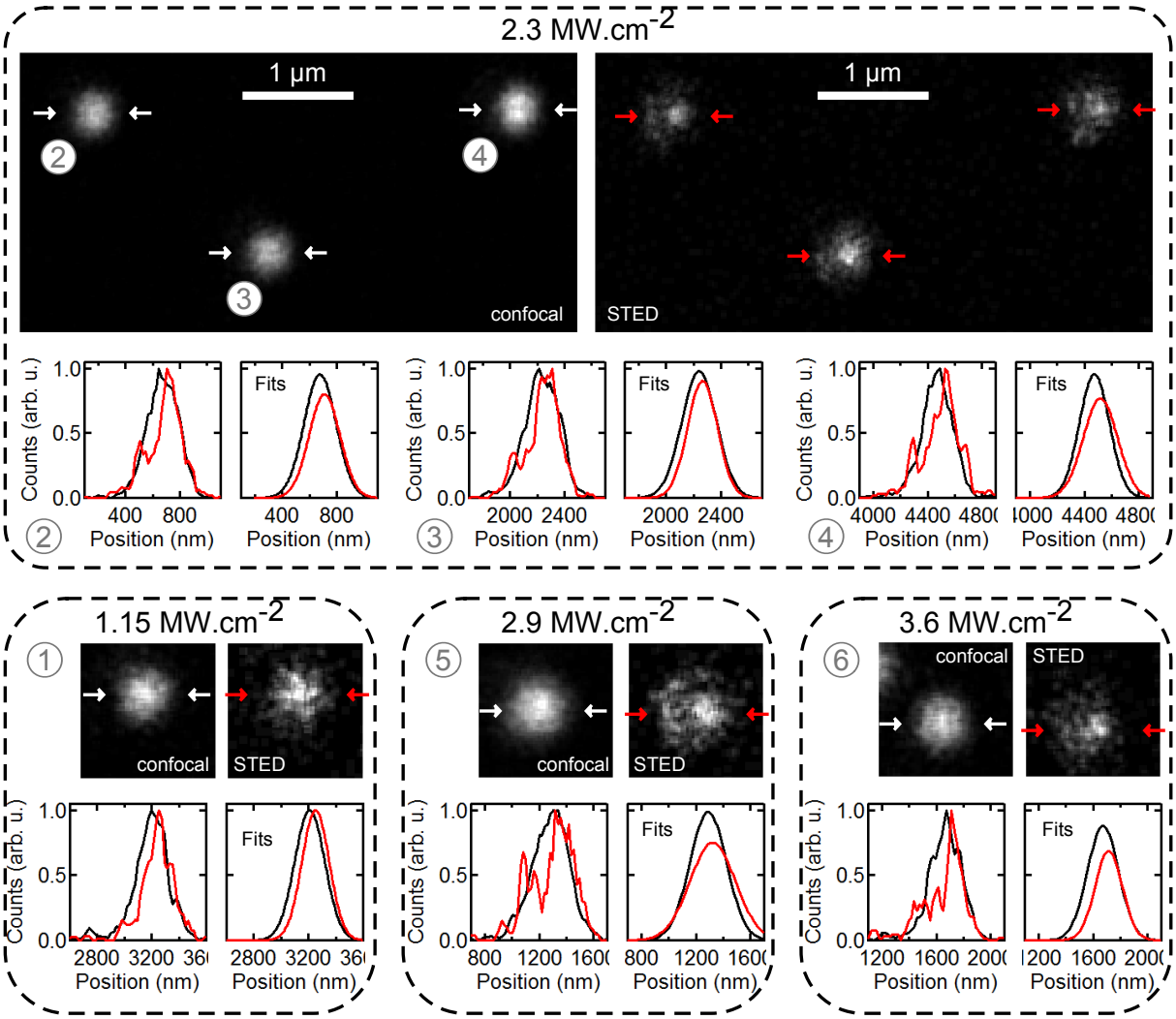


Figure S6: Additional experimental data; horizontal profiles. The labeling 1 through 6 indicates the same NPs as in figure S5.

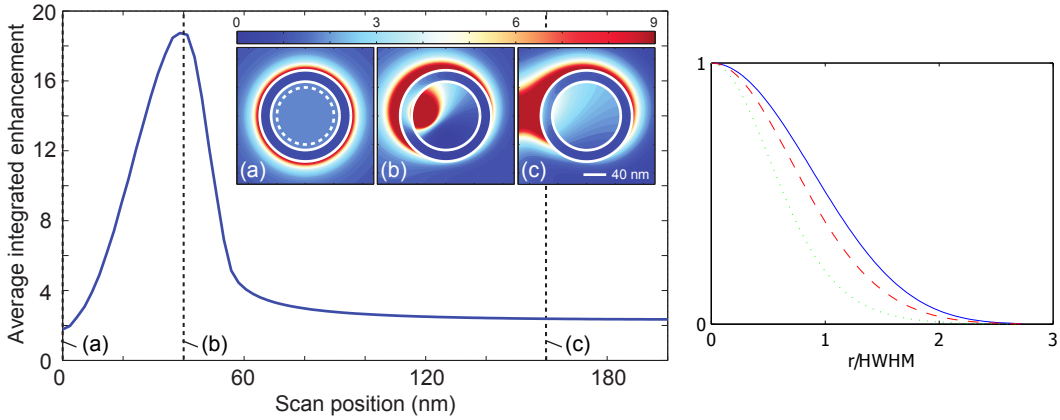


Figure S7: Left: Average intensity enhancement within the core as a function of the scan position. The insets show the complete enhancement distribution for three specific scan positions, indicated by vertical lines ((a), (b) and (c)) in the main plot. The white circles represent the core and shell boundaries whereas the dashed white line (10 nm inside the core) indicates the region beyond which we assumed that no contribution to the fluorescence can arise due to quenching. Right: PSF of a single core-shell fluorescent label calculated with exact Mie formulation.

## References


(1) Auksorius, E.; Boruah, B. R.; Dunsby, C.; Lanigan, P. M. P.; Kennedy, G.; Neil, M. A. A.; French, P. M. W. *Opt. Lett.* **2008**, *33*, 113–115

(2) Lenz, M. O.; Sinclair, H. G.; Savell, A.; Clegg, J. H.; Brown, A. C. N.; Davis, D. M.; Dunsby, C.; Neil, M. A. A.; French, P. M. W. *Journal of Biophotonics* **2014**, *7*, 29–36

(3) Foreman, M. R.; Sivan, Y.; Maier, S. A.; Török, P. *Phys. Rev. B* **2012**, *86*, 155441

(4) Sivan, Y.; Sonnefraud, Y.; Kéna-Cohen, S.; Pendry, J. B.; Maier, S. A. *ACS Nano* **2012**, *6*, 5291–5296

(5) Sivan, Y. *Applied Physics Letters* **2012**, *101*, 021111